Geothermal Energy

RESEARCH Open Access

Cooling-induced permeability enhancement for networks of microfractures in superhot geothermal environments

Ryota Goto[1*], Daisuke Nakayama[1], Ryota Takahashi[1], Eko Pramudyo[1], Kohei Takuma[1] and Noriaki Watanabe[1*]

*Correspondence: ryouta.gotou.q1@dc.tohoku.ac.jp; noriaki.watanabe.e6@tohoku.ac.jp

[1] Department of Environmental Studies for Advanced Society, Graduate School of Environmental Studies, Tohoku University, Sendai 9808579, Japan

Abstract

Recent researches have proposed the use of enhanced geothermal system reservoirs consisting of dense networks of microfractures, created by hydraulic and/or thermal fracturing in superhot/supercritical geothermal environments, because of their suitability for thermal energy harvesting. During fracturing and energy extraction, the fracture networks are exposed to cooling due to the injection of cold fluid into the reservoirs. Previous studies showed such cooling enhanced reservoir permeability in conventional geothermal environments. However, the cooling may result in a higher risk of seismicity, owing to decreased normal stress on the fractures. Nevertheless, it is unclear whether cooling-induced permeability enhancement and a higher risk of seismicity occurs within networks of microfractures which consist of numerous interconnected microfractures at various orientations to the in situ triaxial stress. Thus, no dominant fractures have the possibility to cause permeability enhancement/induced seismicity. In this study, results are presented for borehole cooling experiments on a dense network of microfractures in granite, at 400 °C, under true triaxial stress. Permeability and acoustic emissions were measured with decreases in borehole temperature (up to ~ 90 °C). Results showed that permeability increased with increasing temperature drop at relatively low stress levels (15 and 20 MPa). The permeability enhancement occurred without intensive failure, and was reversible. However, permeability was almost constant at a higher stress level (65 MPa). Results showed that permeability enhancement required a thermal stress equivalent to the mean stress, so that the normal stress was reduced to near-zero, for a considerable amount of the microfractures. Additionally, the permeability of dense microfracture networks can be increased by cooling primarily through thermo-elastic deformation (without intensive failure), which may be useful to compensate for the reduction in injectivity due to cooling-induced fluid property changes.

Keywords: Thermal stress, Permeability, Microfracture network, Supercritical, Superhot, Geothermal, Enhanced geothermal system, Fracturing, Energy extraction

Introduction

Owing to the considerable increase in population growth over the past few decades, there has been an associated increase in demands on renewable energy resources. Furthermore, developing unconventional superhot/supercritical geothermal resources has

been attracting attention in many countries. The conditions required are: to exceed the critical temperatures of water (374 °C for water and 406 °C for seawater) at drillable depths of ~ 2–4 km. Geothermal energy could provide a reliable base load power source as its capability to generate power is independent from weather conditions. Projects exploring superhot geothermal resources have been conducted in Iceland (Friðleifsson et al. 2014; Friðleifsson and Elders 2017; Steingrimsson et al. 1990), Italy (Baron and Ungemach 1981; Batini et al. 1983; Ruggieri and Gianelli 1995; Bertani et al. 2018), Japan (Kato et al. 1998), Mexico (Espinosa-Paredes and Garcia-Gutierrez 2003), and the United States (Fournier 1991; Garcia et al. 2016). The project in Iceland was extremely beneficial because it demonstrated the existence of geothermal reservoirs, which produce water with high specific enthalpy, exceeding 2 MJ/kg (Smith and Shaw 1975, 1978; Friðleifsson and Elders 2005; Tester et al. 2006; Friðleifsson et al. 2007; Elders et al. 2014). Thus, utilization of superhot geothermal resources will play a key role in improving the productivity and sustainability of geothermal energy generation.

However, in superhot geothermal environments in a continental granitic crust, the formation of permeable fracture networks (Tsuchiya et al. 2016; Watanabe et al. 2017a; Weis et al. 2012) can potentially be suppressed by: the increased efficiency of mineral crystal plasticity (Parisio et al. 2019, 2020; Tullis and Yund 1977; Violay et al. 2017); the retrograde solubility of silica minerals (Fournier 1991; Saishu et al. 2014; Tsuchiya and Hirano 2007; Watanabe et al. 2021), and the enhanced rates of fracture healing/sealing caused by water–rock reactions (Moore et al. 1994; Morrow et al. 2001; Watanabe et al. 2020). Therefore, it is important to develop technologies for artificially creating or recreating permeable fracture networks, to establish enhanced geothermal systems (EGS) in superhot geothermal environments. Recent studies have shown that water injection (at or near its critical temperature) into granite can create a dense network of microfractures suitable for geothermal energy extraction. This cloud-fracture network (Fig. 1) is created through continuous infiltration and the stimulation of pre-existing microfractures through low-viscosity water (Goto et al. 2021; Watanabe et al. 2017b, 2019; Liu et al. 2022). Additionally, research suggests that the pore pressure required to initiate this flow-induced microfracturing may be predicted by the Griffith failure criterion, which assumes the initiation of brittle failure from pre-existing fractures. It is a function of the maximum and minimum principal stresses and tensile strength of rocks (Cox 2010; Griffith 1924; Jaeger and Cook 1979; Secor 1965).

These densely distributed microfracture networks may also be created by thermal fracturing (Siratovich et al. 2015; Jin et al. 2019; Shen et al. 2020). The networks are considered desirable for efficient geothermal energy production due to its large heat exchange area. In addition, the isotropic distribution of the fracture network may facilitate the drilling of production wells that connect to the formed fractures. Therefore, an experimental study was conducted to explore the applicability of flow-induced microfracturing over a wider temperature range, including conventional geothermal environments (Pramudyo et al. 2021). The results in this study demonstrated the formation of cloud-fracture networks at 200–450 °C using carbon dioxide as a fracturing fluid, as it has a sufficiently low viscosity at a wide range of temperatures.

Although it is possible to use superhot geothermal resources by means of EGSs, there are some issues. During the creation of a large-scale geothermal reservoir by hydraulic

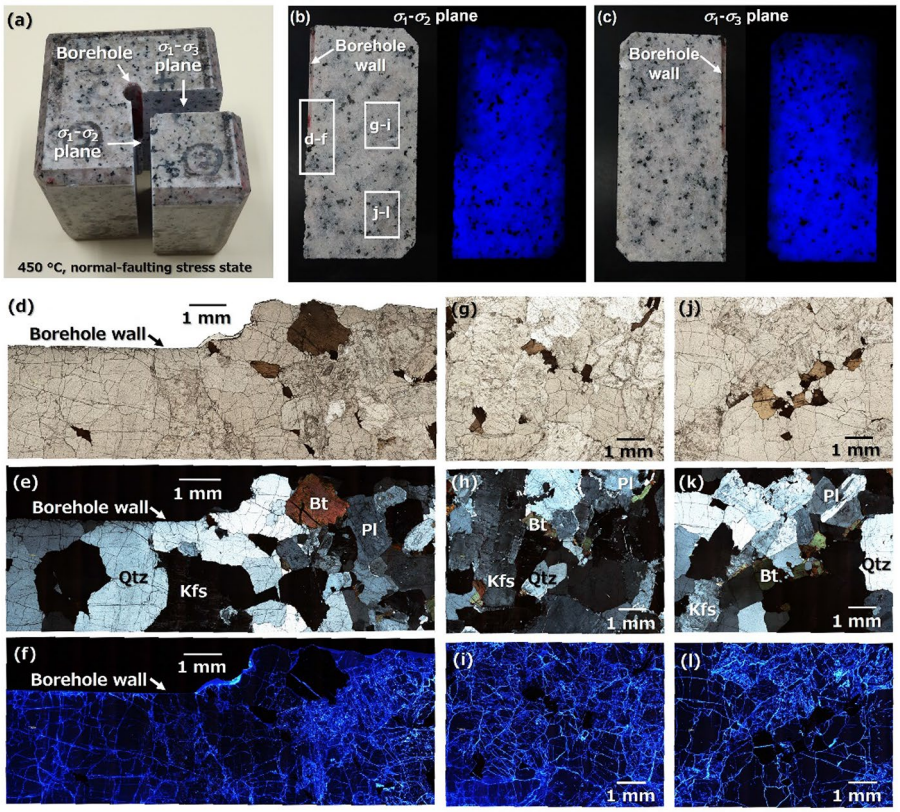

Fig. 1 Complex fracture pattern representing a cloud-fracture network, produced by hydraulic fracturing of granite at 450 °C under true triaxial stress, adapted from Watanabe et al. (2019). The fractured granite impregnated with the fluorescent resin (**a**). Even blue fluorescence over cross-sections of both the σ_1–σ_2 and σ_1–σ_3 planes of the sample (**b**, **c**), where σ_1, σ_2, and σ_3 denote the maximum, intermediate, and minimum principal stresses, respectively. Optical microphotographs of a thin section of the σ_1–σ_2 plane cross-section near and far from the borehole, using uncrossed polarized, crossed polarized and UV light (**d**–**l**)

fracturing, the temperature of water in the injection well decreases with time (Watanabe et al. 2022). Moreover, after creating a geothermal reservoir or enhancing the permeability of existing fractures, prolonged injection of a colder fluid is necessary to exploit thermal energy from the rock. Hence, fractures are being cooled throughout development and production of the geothermal resource. Cooling can induce thermal contraction of the reservoir rock, which may change reservoir permeability, owing to deformation of fractures and/or failure of the rock. For example, a field experiment reported that the injectivity of a well is increased by cold water injection (Grant et al. 2013). Additionally, a numerical study showed that a high-permeability flow path would be formed in a fracture network, owing to cooling-induced fracture opening during exploiting geothermal energy in EGS at conventional geothermal conditions (Sun et al. 2017). Other numerical studies on conventional geothermal environments reported that the thermal contraction may lead to permeability enhancement of existing fractures (Kang et al. 2022). Additionally, it was also showed numerically that permeability enhancement will occur when the induced tensile thermal stress reduces normal stress on a fracture to near-zero (Kaneta et al. 2014). Contrastingly, the thermal contraction may induce seismicity, owing to reduced normal stress (i.e., reduced frictional force) on a fracture. Enhanced geothermal

system projects have been exposed to induced seismicity, even causing suspension of projects (Haring et al. 2008; Deichmann and Giardini 2009; Grigoli et al. 2018; Kim et al.2018) Additionally, a numerical study suggested that thermal contraction-induced seismicity could be more severe in superhot environments owing to larger difference in temperature between the reservoir and injected fluid (Parisio et al. 2019).

A literature review suggested that cooling-induced permeability enhancement may occur, even in superhot geothermal reservoirs consisting of dense network of microfractures, with or without a higher risk of induced seismicity. However, this is unclear, because the networks consist of numerous interconnected microfractures, of various orientations to the true triaxial stress. The networks are quite different from networks of sparsely distributed larger fractures existing in conventional reservoirs, and it is therefore currently difficult to handle theoretically and/or numerically.

This study aims to provide insights into the possibility and characteristics of cooling-induced permeability enhancement in superhot geothermal reservoirs via a set of borehole cooling experiments on cubic granite, containing a dense network of microfractures at 400 °C, under true triaxial stress. Permeability and acoustic emission (AE) were measured with varying decreases in borehole temperature, up to ~ 90 °C. The results of three experiments at different true triaxial stress conditions are provided. Finally, the criteria for permeability enhancement for networks of microfractures are discussed, as well as the importance of cooling superhot EGS reservoirs consisting of networks of microfractures.

Materials and methods

Experimental system

The experimental system used in this study (Fig. 2) was originally developed for supercritical hydraulic fracturing by Watanabe et al. (2019) and applied by Pramudyo et al. (2021); Goto et al. (2021, 2022). The system consisted of a true triaxial cell which contained: a $100 \times 100 \times 100$ mm cubic rock sample; a triaxial loading system; a pump for injecting fracturing fluid into the sample; a pump for injecting confining fluid (high-viscosity plastic melt in this system) along the sample edges via an injector; an elastic wave measurement system, and a temperature control and data logging system. The elastic wave measurement system used was an AE measurement device (Physical Acoustics Cooperation's two-channel data acquisition and digital signal processing AE system, PCI-2).

The true triaxial cell (Fig. 2b, d) included a pressure vessel with a cubic skeleton, six pistons (to apply a compressive load to the cubic rock sample via a copper gasket), a plastic filling (that melts at the experimental temperature to seal the sample edges), a plastic melt injector (to control the plastic melt pressure), and thermal insulators, used in conjunction with heaters, for the pressure vessel. The pressure vessel has six cylindrical holes to allow the pistons to be inserted into the vessel, with graphite packing lubricating the sliding portions, to provide sealing for the plastic melt. The edges of the sample were chamfered (shown in Fig. 2a) so the loading face of the sample corresponded to the dimensions of the copper gasket and loading face of the piston (90×90 mm). Each piston had four cartridge heaters.

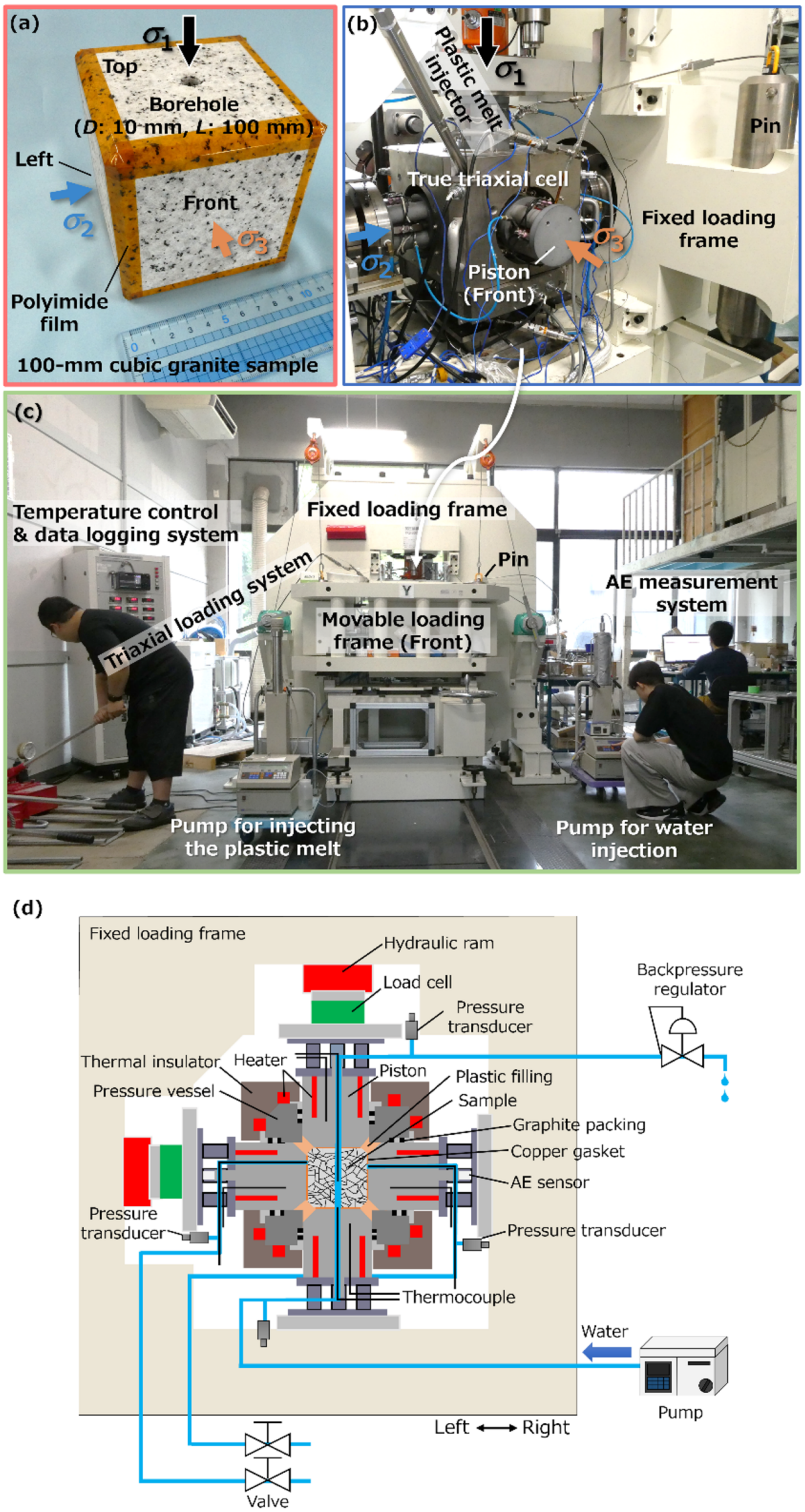

Fig. 2 Photos of the granite sample (**a**), true triaxial cell (**b**), and experimental system in the borehole cooling experiment (**c**), together with a schematic illustration of the experimental system (**d**)

The bottom piston was equipped with a pipe (which acts as a flow path) and a thermocouple, positioned to extend its end to the sample surface. This pipe was connected to a pressure transducer and a pump for water injection. The top piston was also equipped with a pipe and thermocouple, positioned to extend its end to the center of the borehole of the sample. This pipe was connected to a valve and backpressure regulator. Two pairs of horizontal pistons were equipped with pipes, and a thermocouple was positioned to reach the sample surface. It included an elastic wave guide bar on the opposite side of the loading face. Each pipe was connected to a pressure transducer and a valve, where the pressure transducer was placed closer to the piston, so that the fluid pressure at the loading face could be measured when the valve was closed (under undrained conditions). The copper gasket for horizontal pistons had both concentric and radial grooves to collect water from the outlet face area of the sample.

An AE sensor (R15α, 150 kHz resonant frequency sensor, Physical Acoustics Corporation) was attached to the face of the elastic wave guide bar of the two horizontal pistons applying the intermediate principal stress (Fig. 2d). In this study, the maximum, intermediate, and minimum principal stresses were denoted as σ_1, σ_2 and σ_3, respectively. The temperature of the bar was maintained near-room temperature using a cooling jacket, through which water from a chiller circulated.

The plastic filling (Fig. 2d) was polyether ether ketone (PEEK), which has a melting point of 343 °C. Molten PEEK can be injected under a controlled pressure using the injector (Fig. 2b), even with its high viscosity (e.g., 350 Pa·s at 400 °C). A cylindrical PEEK rod (which melts in the vicinity of the pressure vessel) was injected by a metallic piston pushed by water at a constant pressure. To prevent PEEK melt from adhering to rock surfaces, a polyimide film (thickness of ~ 50 μm) was used to cover the edges of the sample, as a release agent (Fig. 2a). Polyimide has no melting point and decomposes at > 500 °C without melting.

As shown in Fig. 2c, the triaxial loading system comprises of a fixed and a movable loading frame. The fixed frame had two hydraulic rams that were placed vertically and horizontally. The movable loading frame had a horizontal hydraulic ram. Each hydraulic ram had a capacity of 3 MN and was actuated with a hand oil pump. The true triaxial cell was carefully placed on a loading platform of the fixed frame to prevent eccentricity of loading, and was connected to the pumps, AE measurement system, and the temperature control and data logging system. When a compressive load was applied, the movable loading frame engaged with the fixed loading frame using four cylindrical pins (Fig. 2b). The triaxial loading system independently applied a compressive load in three orthogonal directions, using a single hydraulic ram with a fixed loading platen on the opposite side. The hydraulic ram, equipped with a load cell, pushed the piston of the true triaxial cell via a spherical seated platen.

Experimental procedure

Once the experimental system was set up, the temperatures of the pressure vessel and pistons were increased to 400 °C, and ~ 50 kN of hydrostatic load was applied to the sample. When the temperatures reached the prescribed value, PEEK melt was injected into the pressure vessel at a pressure of 4 MPa. Subsequently, the sample underwent a true triaxial stress state. Under the prescribed temperature and stress conditions, water was

injected into the borehole from the bottom piston at a set flow rate (1, 5, 10 and 15 mL/min, at room temperature), and then flowed out through the backpressure regulator, at a prescribed pressure. The borehole pressure could not be completely controlled to remain at the desired 1 MPa, but it varied between ~ 1 and 4 MPa. This was owing to an unexpectedly large pressure loss in the pipe, water-steam two-phase flow through the backpressure regulator, and a temperature change of the backpressure regulator. Note that the borehole was cooled by steam at low pressure to minimize influences of opening/closing of fractures by the dissolution/precipitation of minerals as well as pore-pressure induced stress changes. During water injection into the borehole, the change in water pressure (initial value was 0 MPa) was measured at each outlet, at a constant temperature, with a closed valve. Additionally, AE activity was monitored during the injection.

At a decrease in borehole temperature, the permeability in the four horizontal directions was evaluated, based on the borehole pressure (which is ideally constant). The rate of increase in water pressure was calculated by:

$$k_i = \frac{\Delta P}{\Delta t} \times \frac{1}{P_b}, \tag{1}$$

where k_i is permeability index, which was defined as a proxy of permeability; P_b is the borehole pressure, which balances the influences of pressure gradient and effective stress changes, and ΔP is increase in outlet pressure during a time interval (Δt). To use the equation, a time interval (Δt) was selected, during which the borehole temperature and pressure were generally constant. The average borehole pressure and change in outlet water pressure (during the time interval) were P_b and ΔP, respectively.

Experimental conditions

Three 100 × 100 × 100 mm cubic granitic rock samples (Samples 1–3) were prepared for the borehole cooling experiment under true triaxial stress. A single borehole was at the center, with a diameter and length of 10 mm and 100 mm, respectively. After making the borehole, fractures were induced thermally within samples using an electric furnace. The granite was Inada granite from Ibaraki prefecture, Japan, which has been used in previous studies on supercritical hydraulic fracturing, borehole failure experiments, and supercritical carbon dioxide fracturing (Pramudyo et al. 2021; Goto et al. 2021, 2022; Watanabe et al. 2017b, 2019). The tensile strength, compressive strength, Young's modulus, porosity, and intrinsic permeability of the intact granite near atmospheric pressure were 4–9 MPa, 160–180 MPa, 55–80 GPa, 0.5–0.8%, and 2×10^{-18} to 8×10^{-18} m^2, respectively.

The networks of microfractures were formed by heating the rock in an electric furnace at 500 °C, at atmospheric pressure for 10 h. After heating, the porosity of each sample was increased to 1.3–1.5% (the values are listed in Table 1). The formation of microfracture network was indicated by the reduction of P-wave velocity. The P-wave velocity of Inada granite for the intact sample is ~ 3400–4300 m/s (Watanabe et al 2019). The measured values and distributions of P-wave velocity were compared with those of intact sample to confirm the formation of a dense network of microfractures. If the microfracture network exists within samples, the value of P-wave velocity decreased to approximately 2000 m/s (Watanabe et al. 2019; Pramudyo et al. 2021; Goto et al. 2021).

Table 1 *P*-wave velocities (average ± standard deviation) in the three principal stress directions and the porosities for each sample

Sample	Measurement direction	*P*-wave velocity (m/s)	Porosity (%)
Sample 1	σ_1 direction	2220 ± 141	1.5%
	σ_2 direction	1854 ± 33	
	σ_3 direction	2275 ± 38	
Sample 2	σ_1 direction	1920 ± 53	1.5%
	σ_2 direction	1973 ± 34	
	σ_3 direction	2248 ± 53	
Sample 3	σ_1 direction	2001 ± 67	1.3%
	σ_2 direction	2081 ± 32	
	σ_3 direction	2360 ± 48	

The P-wave velocity was measured for each sample under dry, room temperature, and atmospheric pressure conditions. The measurement system consisted of a pulser/receiver, and a laptop computer to obtain the one way travel time (first arrival time) for P-waves transmitted between the two opposite transducers. A P-wave with a relatively low frequency (50 kHz) was chosen to ensure wave propagation through fractured granite. Waves of higher frequencies (~0.1–100 MHz) can suffer larger attenuation in fractured granite (Chaki et al. 2008). Each face of the sample was divided into 3 × 3 pixels. A distance of 100 mm travel time was measured between each of the opposing pixel pairs to compute P-wave velocities. There were total of 27 voxels solved by 27 equations of: $1/V_p = (1/v_{p1} + 1/v_{p2} + 1/v_{p3})/3$; where V_p is the velocity for each pixel pair, and v_{p1}, v_{p2}, and v_{p3} are the velocities for voxels between the pixel pairs.

Table 1 lists P-wave velocities (average ± standard deviation) for three directions parallel to the principal stresses which were applied to the sample. For all samples, average P-wave velocities were approximately 2000 m/s. Similar values have been reported in previous studies for the same type of granite containing cloud-fracture networks (as shown in Fig. 1) after hydraulic fracturing (Watanabe et al. 2019; Goto et al. 2021). However, the standard deviation was smaller for the thermally fractured granite in this study. Figure 3 shows the 3-D distribution of P-wave velocity for each sample, with the homogenous and isotropic distribution of the P-wave velocities. Such P-wave distributions have also been reported for the same type of granite containing cloud-fracture networks (Watanabe et al. 2019; Goto et al. 2021). Dense networks of microfractures were produced in all samples.

Three borehole cooling experiments were conducted (Runs 1–3) using Samples 1–3, respectively (Table 2). In all experiments, the flow rate was increased from 1 to 15 mL/min. This was to investigate the permeability change and intensity of failure, if present, as a function of the decrease in borehole temperature (higher temperature decrease at higher flow rate). It should be noted that water injection was stopped until the borehole temperature returns to the initial value and the injection was restarted with different flow rate. The flow rate was then returned to 1 mL/min to examine reversibility of cooling-induced changes in the rock. Run 1 was conducted with σ_1, σ_2, and σ_3 at 40, 15 and 5 MPa, respectively. This gives a relatively low mean stress of 20 MPa, at which both permeability change and macroscopic failure are likely to occur. Based on a

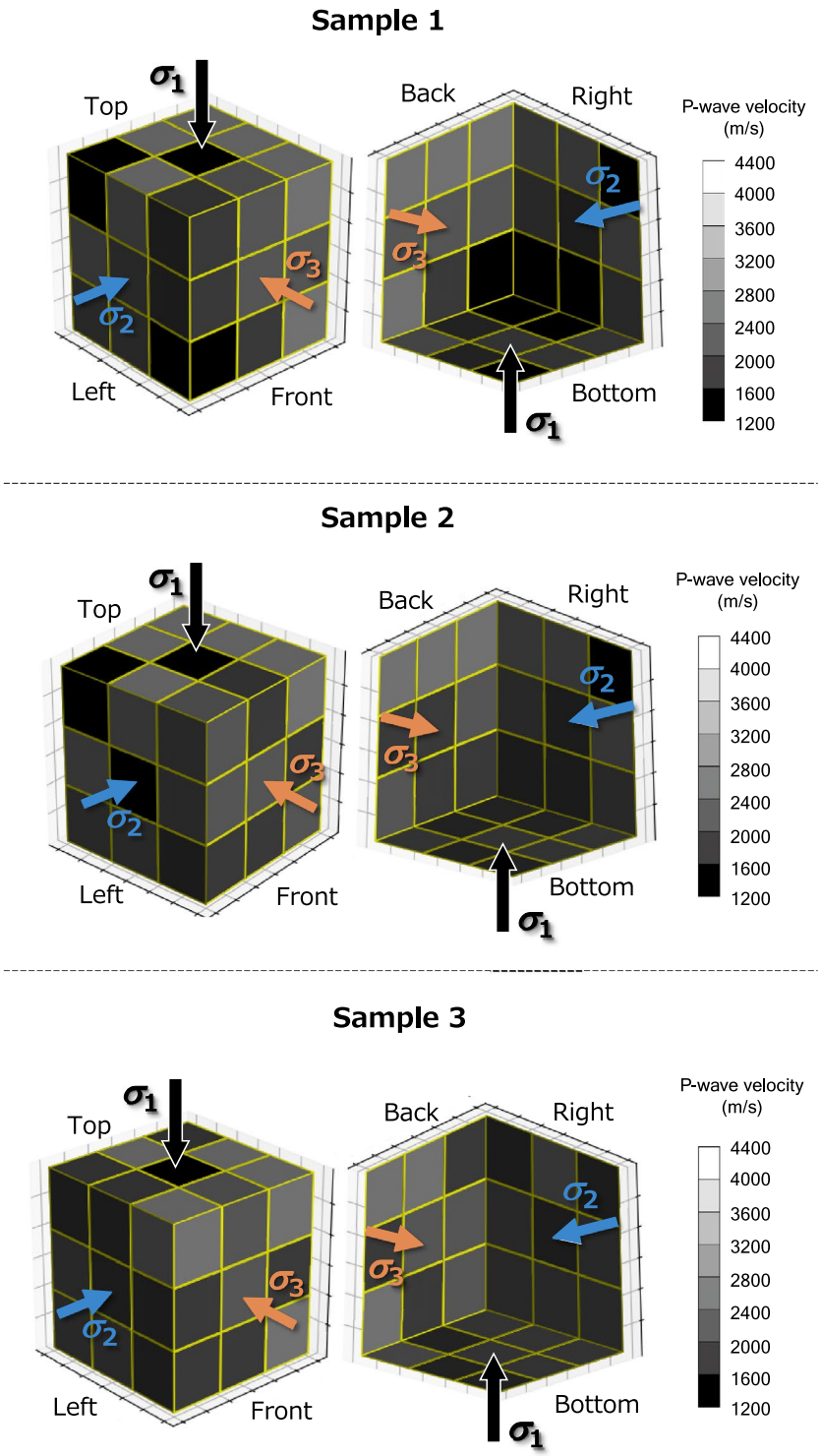

Fig. 3 Estimated P-wave velocity distributions for samples

Table 2 Conditions for each borehole cooling experiment

Experiment	Sample	Stress state $\sigma_1/\sigma_2/\sigma_3$ (MPa)
Run 1	Sample 1	40/15/5
Run 2	Sample 2	85/60/50
Run 3	Sample 3	15/15/15

preliminary assessment, the maximum drop in borehole temperature was ~ 80 °C. At an 80 °C temperature drop, the tensile thermal stress was approximately 50 MPa, based on the following:

$$\sigma_T = \alpha \Delta T E \tag{2}$$

where σ_T is thermal tensile stress; α is thermal expansion coefficient of rock; ΔT is temperature drop, and E is Young's modulus. In this study, the values of α and E were assumed to be 20×10^{-6} K^{-1} and 30 GPa, respectively, based on literature (Heuze 1983; Parisio et al. 2019; Sun et al. 2021). Consequently, in Run 1, normal stress on fractures at various orientations may have reduced to below zero. Run 2 was conducted at a higher mean stress of 65 MPa (i.e., $\sigma_1/\sigma_2/\sigma_3$: 85/60/50 MPa), with the same differential stresses (35 MPa), to demonstrate that permeability enhancement requires near-zero stress on some amount of fractures. Finally, Run 3 was conducted under hydrostatic stress (i.e., $\sigma_1=\sigma_2=\sigma_3=15$ MPa) to explore the influence of normal stress variations on the degree of permeability enhancement. Additionally, this experiment was conducted to demonstrate that shear deformation of fractures is not necessary in the cooling-induced permeability enhancement.

Results and discussion

Cooling-induced permeability enhancement

Figure 4 shows the temporal changes in temperatures and water pressures for the borehole and four outlet faces, as well as the AE energy, for each flow rate in Run 1 (which was conducted at a lower mean stress of 20 MPa). Figure 4 only show results for when the flow rate was initially set to 1 mL/min, and not when it was set back to 1 mL/min after the increase because the results were similar. It should be noted that σ_x (y) in Fig. 4a2, b2, c2, d2 denotes pressure for the outlet face, y, subjected to the principal stress, σ_x.

At the lowest flow rate of 1 mL/min (Fig. 4a1), both the borehole and outlet temperatures remained almost constant. However, higher flow rates introduced higher cooling rate, even though the temperature of water flowing out from the pump was fixed, into the borehole (Fig. 4b1, c1, d1) decreasing the temperature significantly, and then plateaued, although the outlet temperatures remained constant. It was indicated that the temperature drop in the sample was at a maximum in the borehole and decreased to zero at the outlet faces because the temperature drop did not reach the outlet faces of the sample. There were larger differences between initial and plateau temperatures for

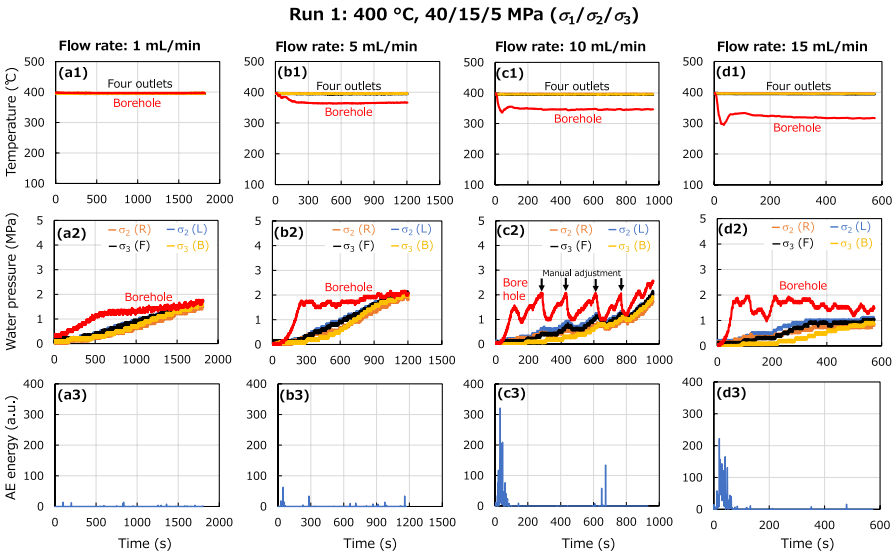

Fig. 4 Temporal changes in temperatures and water pressures for the borehole and four outlet faces, and AE energy at 1 mL/min (a1–a3), 5 mL/min (b1–b3), 10 mL/min (c1–c3), and 15 mL/min (d1–d3) in Run 1. σ_x (y) in the middle row demotes the pressure for the outlet face, y (R: right face, L: left face, F: front face, B: back face) subjected to the principal stress, σ_x (x: 1, 2, 3)

the borehole at a higher flow rate. The temperature drop was ~ 30 °C at 5 mL/min, 50 °C at 10 mL/min, and 80 °C at 15 mL/min.

During the temperature changes, the borehole pressure increased to a constant value in overall trend, except at a flow rate of 10 mL/min (Fig. 4a2, b2, c2, d2). As mentioned in "Experimental procedure" Sect, the borehole pressure did not become 1 MPa as planned, owing to reasons such as unexpectedly large pressure loss in the pipe, water-steam two-phase flow through the backpressure regulator, and temperature change of the backpressure regulator. At 10 mL/min, the pressure was adjusted manually via the backpressure regulator. However, it was still not possible to control the pressure (shown in Fig. 4c2). Note that in the present study the manual pressure adjustment was attempted only at 10 mL/min in Run 1. At all flow rates, the pressure at all outlet faces increased owing to the flow of steam from the borehole to the outlet faces, under undrained condition (Fig. 4a2, b2, c2, d2).

The AE activity tended to become more intense with increasing flow rates (Fig. 4a3, b3, c3, d3). Larger AE energies tended to occur early, when rapid, large temperature drops occurred in the borehole. This implied a fast deformation and/or failure in the vicinity of the borehole, owing to cooling-induced tensile thermal stress. However, it was concluded that substantial failure did not occur because the cooling-induced permeability change observed in the experiment, was found to be reversible (as discussed further below).

The permeability index for each outlet face (subjected to one of three principal stresses) was calculated for each flow rate, using Eq. 1, based on the borehole and outlet pressure data. A time interval (Δt) was selected, during which the borehole temperature and pressure were largely constant. The average borehole pressure and change in outlet pressure during the time interval were then calculated as P_b and ΔP, respectively (Table 3), which also lists corresponding values of the permeability index. The large

Table 3 Time interval (Δt) with start and end values in parentheses, average borehole pressure (P_b), increase in outlet pressure (ΔP), and permeability index (k_i) for each direction at each flow rate in Run 1

Flow rate (mL/min)	Direction	Δt (s)	P_b (MPa)	ΔP (MPa)	k_i (s^{-1})
1 (1st use)	σ_2 (L)	600 (600–1200)	1.3	0.5	6×10^{-4}
	σ_2 (R)	600 (600–1200)	1.3	0.5	6×10^{-4}
	σ_3 (F)	600 (600–1200)	1.3	0.6	8×10^{-4}
	σ_3 (B)	600 (600–1200)	1.3	0.7	9×10^{-4}
5	σ_2 (L)	550 (250–800)	1.6	1.2	1×10^{-3}
	σ_2 (R)	550 (250–800)	1.6	1.0	1×10^{-3}
	σ_3 (F)	550 (250–800)	1.6	1.1	1×10^{-3}
	σ_3 (B)	550 (250–800)	1.6	1.1	1×10^{-3}
15	σ_2 (L)	200 (150–350)	1.6	0.6	2×10^{-3}
	σ_2 (R)	200 (150–350)	1.6	0.5	2×10^{-3}
	σ_3 (F)	200 (150–350)	1.6	0.7	2×10^{-3}
	σ_3 (B)	200 (150–350)	1.6	0.3	9×10^{-4}
1 (2nd use)	σ_2 (L)	500 (1700–2200)	1.5	0.5	7×10^{-4}
	σ_2 (R)	500 (1700–2200)	1.5	0.5	7×10^{-4}
	σ_3 (F)	500 (1700–2200)	1.5	0.6	8×10^{-4}
	σ_3 (B)	500 (1700–2200)	1.5	0.7	9×10^{-4}

σ_x (y) in the second column denotes the outlet face, y (R: right face, L: left face, F: front face, B: back face) subjected to the principal stress, σ_x (x: 1, 2, 3)

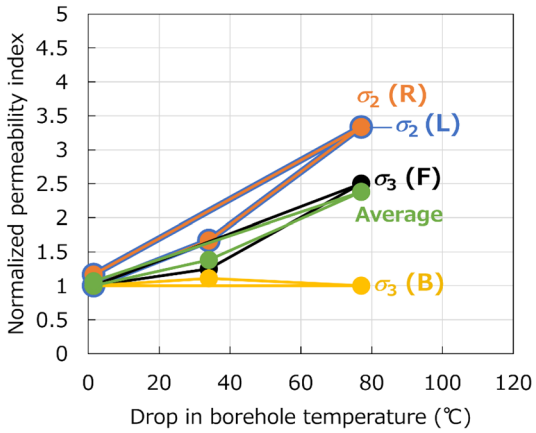

Fig. 5 Relationship between the normalized permeability index and drop in borehole temperature for each direction in Run 1. σ_x (y) denotes the outlet face, y (R: right face, L: left face, F: front face, B: back face) subjected to the principal stress, σ_x (x: 1, 2, 3)

fluctuation in borehole pressure made it impossible to calculate the permeability index for 10 mL/min, and therefore it is not included in the table.

To examine the relationship between permeability in each direction, and the degree of cooling in the experiment, the permeability index, as a function of drop in borehole temperature, is shown in Fig. 5. The permeability index in each direction was normalized by the permeability index for the first use at 1 mL/min. The drop in borehole temperature was the average value during the time interval in the permeability index calculation (Table 3). The average values of permeability indices for all directions are also shown

in Fig. 5. Barring σ_3 (B), all directions showed the permeability index increased with an increase in the drop in temperature. The increase in the average value was ~ 2.4 times at a temperature decrease of ~ 80 °C. Therefore, the overall permeability of the sample increased with increasing degrees of cooling, demonstrating the occurrence of cooling-induced permeability enhancement of the network of microfractures. Since the permeability indices at the near-zero temperature drop both uses of 1 mL/min were very similar, this demonstrates that substantial failure did not occur. Therefore, the permeability enhancement was caused primarily by thermo-elastic normal and/or shear deformation of fractures, where the normal stress (frictional force) decreased due to thermal contraction via cooling. Notably, there was no clear relationship between permeability enhancement and the principal stress direction. The permeability indexes for σ_3 (F) and σ_3 (B) showed entirely different changes, despite the same principal stress direction, owing to the characteristics of the network of microfractures, which consisted of numerous fractures at various orientations.

According to a numerical study (Kaneta et al. 2014), the enhancement of cooling-induced permeability of a fracture will occur when the induced tensile thermal stress reduces the normal stress on the fracture to a near-zero value. To examine this for the network of microfractures, Run 2 was conducted at higher mean stress of 65 MPa. Figure 6 shows the temporal changes in temperatures, and water pressure for the borehole and the four outlet faces, as well as the AE energy, for each flow rate in Run 2. Changes in both borehole and outlet temperatures were qualitatively similar to those in Run 1 (Fig. 6a1, b1, c1, d1). The temperature drop was approximately 30 °C at 5 mL/min, 60 °C at 10 mL/min, and 80 °C at 15 mL/min. As in Run 1, it was difficult to control the borehole pressure using the back pressure regulator (Fig. 6a2, b2, c2, d2). Additionally,

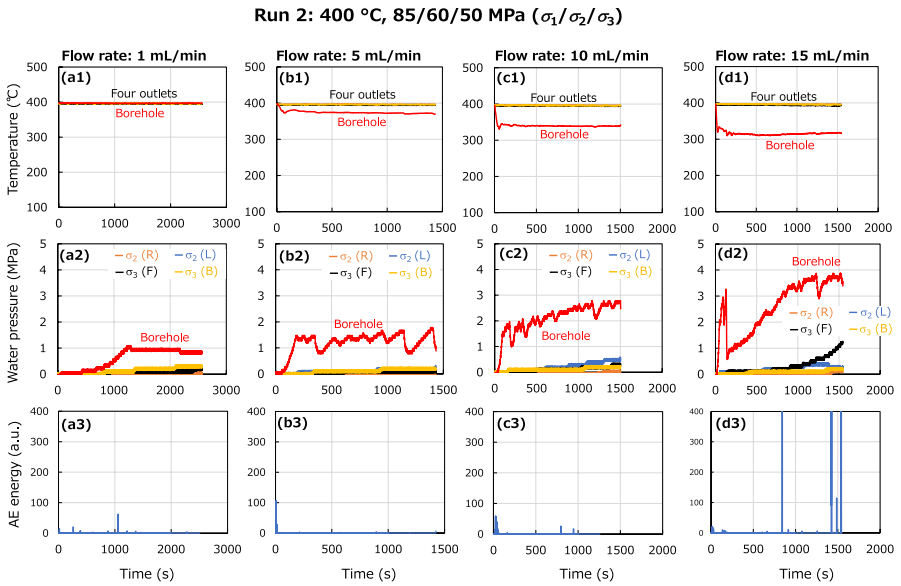

Fig. 6 Temporal changes in temperatures and water pressures for the borehole and four outlet faces, and AE energy at 1 mL/min (a1–a3), 5 mL/min (b1–b3), 10 mL/min (c1–c3), and 15 mL/min (d1–d3) in Run 2. σ_x (y) in the middle row denotes pressure for the outlet face, y (R: right face, L: left face, F: front face, B: back face) subjected to the principal stress, σ_x (x: 1, 2, 3)

AE activity tended to become more intensive with an increasing flow rate (Fig. 6a3, b3, c3, d3. However, the AE energies in the initial stages were smaller than those in Run 1, reflecting a smaller impact of cooling-induced tensile thermal stress under the higher principal stress level. Contrary to Run 1, at 15 mL/min, particularly large AE energies occurred sparsely, likely due to occurrence of a failure. However, no substantial failure occurred because the permeability change was largely reversible.

The permeability index for each outlet face (subjected to one of three principal stresses) was calculated for each flow rate. Table 4 summarizes the calculation values and results for Run 2. Figure 7 shows the normalized permeability index as a function of drop in borehole temperature. The permeability index in each direction did not change systematically with the increasing temperature drop. Additionally, the average permeability index did not increase with the increasing temperature drop but remained constant in overall trend. The permeability changes observed in Run 2 were largely reversible (similar to Run 1).

Run 2 showed a maximum temperature drop of ~ 80 °C, with a maximum tensile thermal stress of ~ 50 MPa (based on Eq. 2), which was very similar to σ_3. Consequently, limited fractures at directions perpendicular to σ_3 (or similar) were subjected to near-zero normal stress. Therefore, it was shown that, for the network of microfractures, permeability enhancement required near-zero stress on more fractures. Additionally, shear deformation (non-extensional deformation) of fractures subjected to non-zero normal stress did not contribute significantly to permeability enhancement. However, such

Table 4 Time interval (Δt) with start and end values in parentheses, average borehole pressure (P_b), increase in outlet pressure (ΔP), and permeability index (k_i) for each direction at each flow rate in Run 2

Flow rate (mL/min)	Direction	Δt (s)	P_b (MPa)	ΔP (MPa)	k_i (s^{-1})
1 (1st use)	σ_2 (L)	1350 (1200–2550)	0.9	0.3	2×10^{-4}
	σ_2 (R)	1350 (1200–2550)	0.9	0.1	8×10^{-5}
	σ_3 (F)	1350 (1200–2550)	0.9	0.1	8×10^{-5}
	σ_3 (B)	1350 (1200–2550)	0.9	0.3	2×10^{-4}
5	σ_2 (L)	1200 (200–1400)	1.3	0.2	1×10^{-4}
	σ_2 (R)	1200 (200–1400)	1.3	0	0
	σ_3 (F)	1200 (200–1400)	1.3	0	0
	σ_3 (B)	1200 (200–1400)	1.3	0.2	1×10^{-4}
10	σ_2 (L)	800 (700–1500)	2.5	0.3	2×10^{-4}
	σ_2 (R)	800 (700–1500)	2.5	0.1	5×10^{-5}
	σ_3 (F)	800 (700–1500)	2.5	0.3	2×10^{-4}
	σ_3 (B)	800 (700–1500)	2.5	0.1	5×10^{-5}
15	σ_2 (L)	700 (800–1500)	3.7	0.1	4×10^{-5}
	σ_2 (R)	700 (800–1500)	3.7	0.2	8×10^{-5}
	σ_3 (F)	700 (800–1500)	3.7	0.9	3×10^{-4}
	σ_3 (B)	700 (800–1500)	3.7	0	0
1 (2nd use)	σ_2 (L)	900 (1400–2300)	1.1	0.2	2×10^{-4}
	σ_2 (R)	900 (1400–2300)	1.1	0.1	1×10^{-4}
	σ_3 (F)	900 (1400–2300)	1.1	0.1	1×10^{-4}
	σ_3 (B)	900 (1400–2300)	1.1	0	0

σ_x (y) in the second column denotes the outlet face, y (R: right face, L: left face, F: front face, B: back face) subjected to the principal stress, σ_x (x: 1, 2, 3)

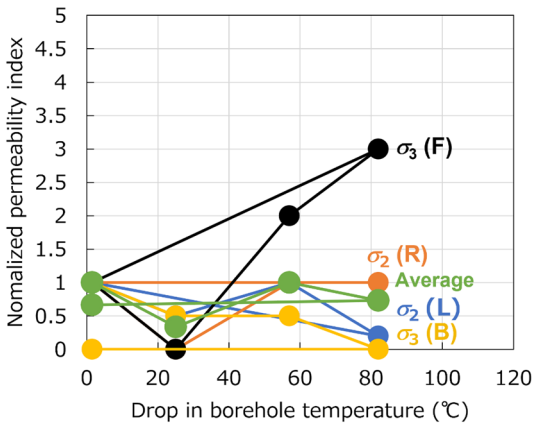

Fig. 7 Relationship between the normalized permeability index and drop in borehole temperature for each direction in Run 2. σ_x (y) denotes the outlet face, y (R: right face, L: left face, F: front face, B: back face) subjected to the principal stress, σ_x (x: 1, 2, 3)

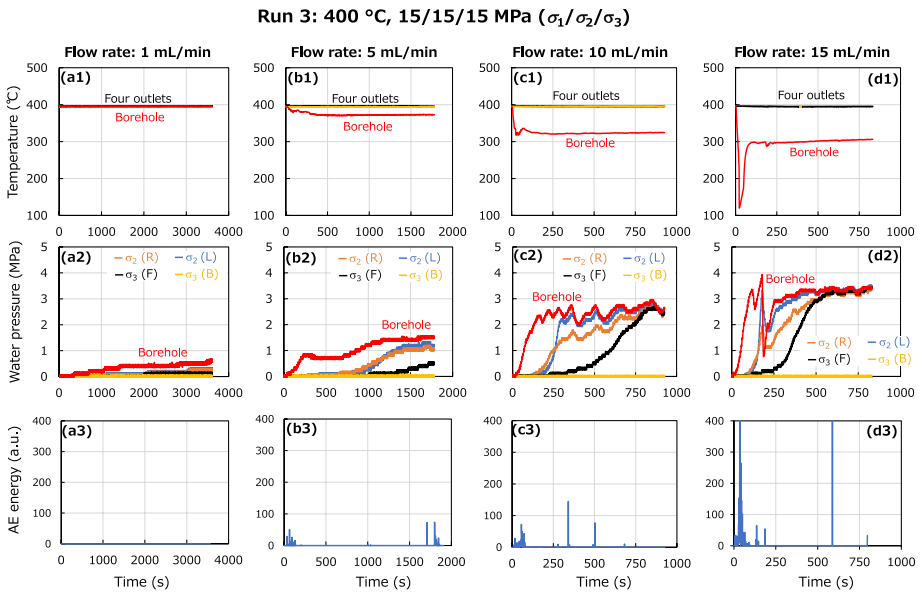

Fig. 8 Temporal changes in temperatures and water pressures for the borehole and four outlet faces, and AE energy at 1 mL/min (a1–a3), 5 mL/min (b1–b3), 10 mL/min (c1–c3), and 15 mL/min (d1–d3) in Run 3. σ_x (y) in the middle row denotes pressure for the outlet face, y (R: right face, L: left face, F: front face, B: back face) subjected to the principal stress, σ_x (x: 1, 2, 3)

shear deformation may have changed flow paths in the network, resulting in complex changes in permeability indexes.

Based on the results, it was hypothesized that a larger permeability enhancement was expected for a smaller variation in normal stress on fractures, at a smaller differential stress, because near-zero normal stress occurred at various locations simultaneously. To examine this hypothesis, Run 3 was conducted under hydrostatic stress (i.e., $\sigma_1 = \sigma_2 = \sigma_3 = 15$ MPa) to explore the influence of normal stress variations on the degree of permeability enhancement. Figure 8 shows the temporal changes in temperature and water pressures and AE energy at each flow rate in Run 3. Changes in both borehole

and outlet temperatures were qualitatively similar to those in Run 1 (Fig. 8a1, 8b1, 8c1, and 8d1). The temperature drop was ~ 20 °C at 5 mL/min, 70 °C at 10 mL/min, and 90 °C at 15 mL/min. The tensile thermal stress was ~ 12 MPa at the smallest temperature drop, and similar to the applied stress. Again, it was difficult to control the borehole pressure via the back pressure regulator (Fig. 8a2, b2, c2, d2). The AE activity became more intensive with an increasing flow rate, and larger AE energies occurred more frequently in the initial stages (Fig. 6a3, b3, c3, d3). At 15 mL/min, a particularly strong AE energy occurred instantaneously. However, despite AE activities, no substantial failure occurred, because the cooling-induced permeability change was reversible.

The permeability index for each outlet face was calculated for each flow rate. Table 5 summarizes the calculation values and results for Run 3, and Fig. 9 shows the normalized permeability index. The permeability index in each direction generally increased with increasing temperature drop, and the cooling-induced permeability change was reversible in all directions. The permeability enhancement occurred anisotropically, even under the hydrostatic stress, thereby reiterating that there was no clear relation between permeability enhancement and the principal stress direction (as observed in Run 1). The average permeability index increased with an increasing temperature drop, and the permeability enhancement was much larger than that in Run 1. For example, the average permeability index in Run 3 was ~ 4, even at a temperature drop of ~ 20 °C, while it in Run 1 was ~ 2.4 at the maximum temperature drop of ~ 80 °C. Therefore, it was demonstrated that a larger permeability enhancement occurred for a smaller variation

Table 5 Time interval (Δt) with start and end values in parentheses, average borehole pressure (P_b), increase in outlet pressure (ΔP), and permeability index (k_i) for each direction at each flow rate in Run 3

Flow rate (mL/min)	Direction	Δt (s)	P_b (MPa)	ΔP (MPa)	k_i (s^{-1})
1 (1st use)	σ_2 (L)	2100 (1500–3600)	0.4	0.2	2×10^{-4}
	σ_2 (R)	2100 (1500–3600)	0.4	0.2	2×10^{-4}
	σ_3 (F)	2100 (1500–3600)	0.4	0.1	1×10^{-4}
	σ_3 (B)	2100 (1500–3600)	0.4	0	0
5	σ_2 (L)	1270 (500–1770)	1.2	1.2	8×10^{-4}
	σ_2 (R)	1270 (500–1770)	1.2	1.1	7×10^{-4}
	σ_3 (F)	1270 (500–1770)	1.2	0.5	3×10^{-4}
	σ_3 (B)	1270 (500–1770)	1.2	0	0
10	σ_2 (L)	700 (200–900)	2.5	2.6	1×10^{-3}
	σ_2 (R)	700 (200–900)	2.5	2.2	1×10^{-3}
	σ_3 (F)	700 (200–900)	2.5	2.6	1×10^{-3}
	σ_3 (B)	700 (200–900)	2.5	0	0
15	σ_2 (L)	560 (250–810)	3.2	1.1	1×10^{-3}
	σ_2 (R)	560 (250–810)	3.2	1.8	2×10^{-3}
	σ_3 (F)	560 (250–810)	3.2	2.9	3×10^{-3}
	σ_3 (B)	560 (250–810)	3.2	0	0
1 (2nd use)	σ_2 (L)	1600 (2000–3600)	1.0	0.7	4×10^{-4}
	σ_2 (R)	1600 (2000–3600)	1.0	0.5	3×10^{-4}
	σ_3 (F)	1600 (2000–3600)	1.0	0.3	2×10^{-4}
	σ_3 (B)	1600 (2000–3600)	1.0	0	0

σ_x (y) in the second column denotes the outlet face, y (R: right face, L: left face, F: front face, B: back face) subjected to the principal stress, σ_x (x: 1, 2, 3)

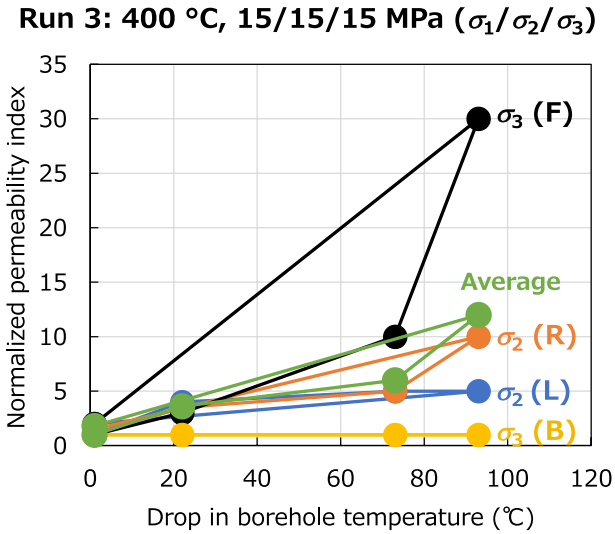

Fig. 9 Relationship between the normalized permeability index and drop in borehole temperature for each direction in Run 3. σ_x (y) denotes the outlet face, y (R: right face, L: left face, F: front face, B: back face) subjected to the principal stress, σ_x (x: 1, 2, 3)

in normal stress on fractures at a smaller differential stress, because near-zero normal stress occurred at a larger number of locations simultaneously. Moreover, it was demonstrated that shear deformation (including extensional deformation) was not necessary to enhance permeability of the microfracture network.

Criteria for permeability enhancement

Results showed that permeability enhancement of the microfracture network required near-zero normal stress on a considerable number of fractures. Additionally, shear deformation of fractures did not contribute significantly to the permeability enhancement. This study further analyzed the criteria for the cooling-induced permeability enhancement in the microfracture network using the following procedure. First, the temperature distribution and corresponding thermal stress within the sample in Run 1 was estimated, based on an unsteady-state heat conduction analysis in 1-D, from the borehole to outlet surface (45 mm length) and Eqn. 2. Then, the tensile thermal stress value, σ_{Tcrit}, at which a positive relationship between the normalized permeability index (Fig. 5) and the distance from borehole with thermal stresses of $\sigma_{\mathrm{T}} \geq \sigma_{\mathrm{Tcrit}}$, was determined. Finally, the initial Mohr's circles ($\sigma_1/\sigma_2/\sigma_3$: 40/15/5 MPa, mean stress: 20 MPa) were moved to the left (lower normal stress side) by the thermal stress of σ_{Tcrit}, to determine the amount of microfractures that satisfied near-zero normal stress conditions.

Assuming negligible heat convection owing to a small volume of water in the fractures, a 1-D (x-direction) unsteady-state heat conduction analysis was performed using the following:

$$\rho c_p \frac{\partial T}{\partial t} = \lambda \frac{\partial^2 T}{\partial x^2}, \tag{3}$$

where ρ is the density; c_p is the specific heat at constant pressure, and λ is the thermal conductivity of the rock; the values used in the analysis were 2560 kg m^{-3},

1080 J kg^{-1} K^{-1}, and 1.3 W m^{-1} K^{-1}, respectively. These values were based on density measurements, and literature for the thermal properties of the Inada granite (Shimada and Hokao 1980). Equation 3 was solved using a finite difference method, with constant temperature boundary conditions of 400 °C, minus the temperature drop in Fig. 5 at $x=0$ mm, and 400 °C, at $x=45$ mm, with initial conditions of 400 °C, at $0<x<45$ mm. The analysis duration was equal to the time interval in the permeability index calculation (Δt in Table 3). Figure 10 shows the final distributions of the estimated temperatures and corresponding thermal stress within the sample at each flow rate for Run 1, in the heat conduction analysis. According to the projected temperature distribution, the distance indicating temperature reduction was greatest at 5 ml/min injection. Comparing the permeability index at 15 ml/min with that of 5 ml/min, it was implied that permeability enhancement requires increasing the distance from borehole at which sufficiently large thermal stress occur. Thus, it was assumed that the thermal stress has to be greater than a certain degree (σ_{Tcrit}) and thermal stress at that value has to reach further from borehole. Four values (5, 10, 15, and 20 MPa) of σ_{Tcrit} were examined as provisional values to cause significant permeability enhancement. Therefore, the correlation between the distance from borehole at $\sigma_T \geq \sigma_{Tcrit}$ and the permeability index was examined.

Figure 11 shows the relationship between the normalized permeability index and distance from the borehole, at $\sigma_T \geq \sigma_{Tcrit}$. Four values of σ_{Tcrit} were tested: 5, 10, 15 and 20 MPa. The procedure to examine the relationship between the permeability index and the σ_{Tcrit} is noted. First, the distance at the $\sigma_T \geq \sigma_{Tcrit}$ with four provisional values at each flow rate (1, 5, and 15 mL/min) is extracted from Fig. 10. Next, the graph was plotted with the values of distances and the permeability indices at each flow rate. Thus, the relationship between the permeability index and the distance where the $\sigma_T \geq \sigma_{Tcrit}$ was examined to derive the plausible value of σ_T to cause significant permeability enhancement. There was a clear positive relationship between the permeability index and distance from the borehole only at $\sigma_{Tcrit}=20$ MPa (which is equal to the mean stress). If the positive correlations between the permeability and the distance from the borehole at σ_T of 10 MPa and 15 MPa were extrapolated, the permeability could rapidly increase

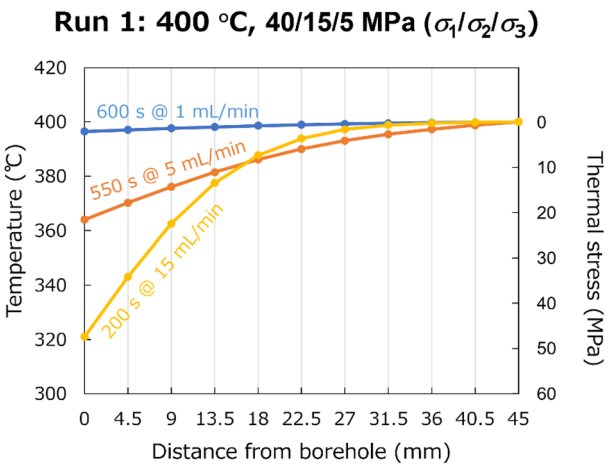

Fig. 10 Final distributions of the estimated temperature and corresponding thermal stress within the sample at each flow rate in Run 1, in the heat conduction analysis

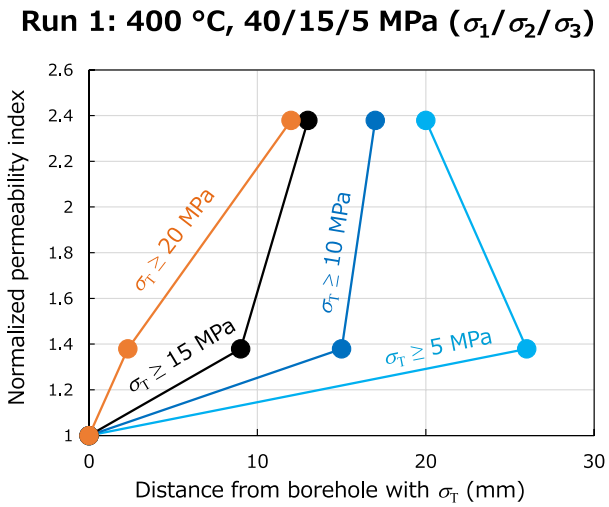

Fig. 11 Relationship between the normalized permeability index and distance from borehole at $\sigma_T \geq \sigma_{Tcrit}$ (= 5, 10, 15 and 20 MPa). The distance where σ_T is bigger than σ_{Tcrit} was extracted from the Fig. 10 at each flow rate. Graph was plotted with the value of permeability index and the distance at each flow rate

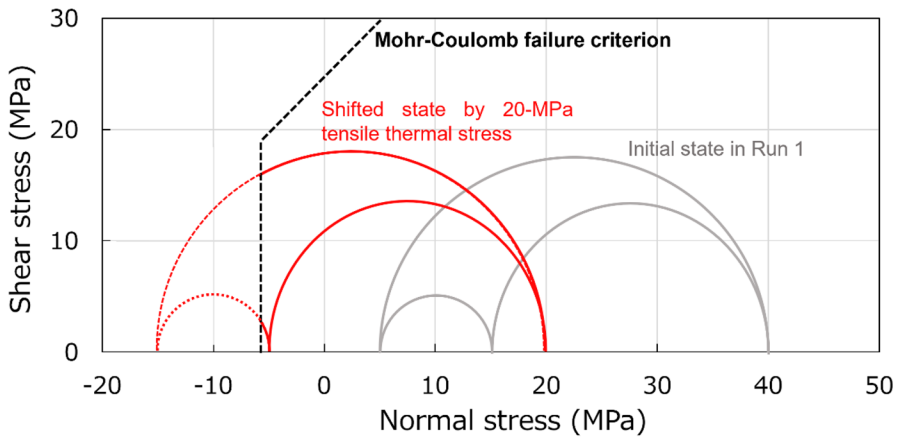

Fig. 12 Mohr's circles at the initial state in Run 1 ($\sigma_1/\sigma_2/\sigma_3$: 40/15/5 MPa), and its horizontal shift by 20 MPa tensile thermal stress

with the distance from borehole despite being lower than the mean stress. However, the increase trend of 20 MPa gradually diminish with the distance. Therefore, the degree of cooling-induce permeability enhancement in Run 1 was dependent on the rock volume which was subjected to a tensile thermal stress of ≥ 20 MPa. Therefore, a thermal stress of 20 MPa was necessary to create higher-permeability flow paths in the network, by reducing normal stress of a sufficient number of fractures to a near-zero value.

Figure 12 shows the Mohr's circles at the initial state in Run 1 ($\sigma_1/\sigma_2/\sigma_3$: 40/15/5 MPa, respectively, and mean stress: 20 MPa), and its horizontal shift by the 20 MPa tensile thermal stress. And the Mohr–coulomb failure criterion at 400 °C. Considering the temperature dependence, the tensile strength, cohesion strength and coefficient of friction were estimated as 7 MPa, 25 MPa, and ~ 0.7, respectively. (Heuze 1983; Kinoshita et al. 1997; Goto et al. 2021). The figure shows combinations of shear and normal stresses in

the three circles. The regions enclosed by these circles represent possible stress states within the sample, and therefore, possible stress states for microfractures. This is because microfractures were densely distributed at various orientations within the sample. Considering the estimated Mohr–Coulomb failure criterion, the tensile failure could occur at some locations. However, the permeability of the rock sample showed reversibility. Thus, it is considered that the substantial failure did not occur. The possible consideration is that the rock sample could accept larger deformation than an intact sample due to the thermally induced fractures. Additionally, the tensile failure perhaps occurred at limited locations. However, the fractures newly created by cooling would not contribute to the permeability enhancement because there were already so many fractures and the permeability enhancement was controlled by such fractures. With a 20 MPa tensile thermal stress, approximately half of the possible stress states were at near-zero normal stress. It was concluded that approximately half of the microfractures need to meet near-zero normal stress, which can be satisfied by inducing thermal stress equivalent to the mean stress. Although this needs validation (for example, by another study), it is reasonable to conclude that the permeability of considerable numbers of the microfractures must be enhanced to cause the permeability enhancement of the network of microfractures.

Implications of permeability enhancement in superhot EGSs

This study clarified the possibility of permeability enhancement of microfracture networks in granite, which potentially comprise reservoirs in superhot EGSs, primarily by thermo-elastic opening (not shear deformation but normal deformation) of the fractures without intensive failure during the cooling of the network. It also provided an empirical criterion for the tensile thermal stress for permeability enhancement. This section discusses the importance of the cooling-induced permeability enhancement in creating EGS reservoirs, and thermal energy extraction from the reservoirs, both of which involve injection of cold fracturing fluid or heat transmit fluid.

A granitic superhot geothermal environment is considered to be at 400 °C, with a pore pressure of 30 MPa, where σ_1, σ_2 and σ_3 were 128 MPa, 112 MPa, and 80 MPa, respectively. The stress values are based on the principal stresses at a depth of 2,937 m for the WD-1a well in the Kakkonda geothermal field, Japan, where the temperature in the well reached ~ 380 °C at 3,100 m (NEDO, 1996; Watanabe et al. 2022). Effective normal stresses based on the values of the pore pressure and principal stresses were 98 MPa (128–30 MPa), 82 MPa (112–30 MPa), and 50 MPa (80–30 MPa). Based on the criterion proposed in this study, permeability enhancement of networks of microfractures occurs when tensile thermal stress reaches 77 MPa, which is equal to the average of the effective normal stresses, by cooling of a fractured rock. According to Eq. 2, this thermal stress may be achieved by a temperature drop of 128 °C. This decrease in temperature is not vast, and it corresponds with a temperature drop from 400 °C to 272 °C. Consequently, injecting fluid at 100 °C, for example, is sufficient to induce the cooling-induced permeability enhancement. Additionally, the permeability enhancement factor may reach several times or larger, based on the results in Run 1 (Fig. 5).

This cooling-induced permeability enhancement is comparable to the reduction in injectivity in mass flow rate due to cooling-induced changes in fluid viscosity and density

during the cold fluid injection for hydraulic fracturing and thermal energy extraction. Based on the Darcy's law in a radial flow from an injection well, the mass flow rate (Q_m), is proportional to a product of the rock permeability (k), a ratio of density to viscosity of the fluid (ρ_f/μ), and a pressure gradient (dP/dr). This can also be written as a product of the permeability, a reciprocal of kinematic viscosity of the fluid (ν^{-1}), and the pressure gradient, as follows:

$$Q_m \propto k\frac{\rho_f}{\mu}\frac{dP}{dr} = k\nu^{-1}\frac{dP}{dr}. \tag{4}$$

Consequently, if the permeability is constant during the cooling of the rock, the mass flow rate decreases with increasing kinematic viscosity, unless injection pressure increases. For example, assuming that temperature in an injection well decreases from 400 °C to 100 °C, during thermal energy extraction by water injection at 30–100 MPa, the mass flow rate of water may decrease by a factor of approximately three, due to the temperature drop. This is because the kinematic viscosity of water increases from $\sim 1\times10^{-7}$ m^2/s at 400 °C, to $\sim 3\times10^{-7}$ m^2/s at 100 °C. Therefore, the cooling-induced changes in fluid density and viscosity causes concern regarding pushing the fracturing front away from the injection well. Additionally, the changes concern the controlling and balancing production and injection rates (i.e., profitable, and sustainable geothermal power generation). However, the cooling-induced permeability enhancement observed in this study has a potential to balance out the adverse influence of cooling-induced fluid property changes. It is therefore recommended that extensive studies are conducted on cooling-induced permeability enhancement for the networks of microfractures in superhot geothermal environments. However, these may be limited to numerical studies because experimental studies are challenging and may not fully address the cooling-induced mechanical and hydraulic responses, which occur in an actual superhot EGS.

Conclusions

This study was novel in that experiments were used to investigate the possibility and characteristics of cooling-induced permeability enhancement for dense networks of microfractures. In granitic superhot/supercritical geothermal environments, such fracture networks, created by hydraulic and/or thermal stimulations, are considered suitable for thermal energy extraction from the environments. A set of borehole cooling experiments on thermally fractured granite were carried out, which contained densely distributed microfractures. Conditions were at 400 °C, and under true triaxial stress. Results showed that significant permeability enhancement occurred without intensive failure that imply the significant increase of the risk of induced seismicity, and the permeability enhancement was larger for a larger degree of cooling. Additionally, the permeability enhancement was primarily caused by reversible thermo-elastic opening, through normal deformation of microfractures, rather than shear deformation. This was triggered by cooling-induced tensile thermal stress, which is a reduction in normal stress for the fractures. There was no clear relationship between permeability enhancement and principal stress directions, which may be attributed to the various orientations of the microfractures. Owing to the presence of these microfractures, the permeability enhancement

of the network required a considerable amount of the fractures to be subjected to near-zero normal stress, to form higher-permeability flow paths. Empirically, this criterion was satisfied when the thermal stress reached the mean stress.

In creating EGS reservoirs and extracting the geothermal energy, it is necessary to inject fluids, which causes the temperature drop of the fluid in the injection well. However, this creates a concern over a reduction in injectivity, owing to cooling-induced changes in fluid density and viscosity. For example, the injectivity of water was estimated to decrease by a factor of approximately three, when assuming a temperature drop from 400 °C to 100 °C, at 30–100 MPa. However, the cooling-induced permeability enhancement observed in this study, has the potential to compensate the loss of injectivity due to the changes in the fluid properties. Therefore, further studies are required in future with particular focus on muti-scale and multi-physics simulations in superhot/supercritical geothermal environments, such as a reservoir under higher stress state, where heat advection is caused by fluids injected with higher pressure. This will aid in better understanding and realization of profitability and sustainability of superhot/supercritical-enhanced geothermal systems.

Abbreviations

AE	Acoustic emission
EGS	Enhanced geothermal system

Acknowledgements
The authors would also like to thank Toei Scientific Industrial Co., Ltd., for manufacturing the experimental system.

Author contributions
RG and DN designed the overall study under the supervision of NW. RG, DN, RT, EP and KT performed the experiments. RG, DN and NW analyzed the results and drafted the manuscript. All authors read and approved the final manuscript.

Funding
This study was supported in part by the Japan Society for the Promotion of Science (JSPS) through Grants-in-Aid for Scientific Research (B) [Grant Number 22H02015], Challenging Research (Pioneering) [Grant Number 21K18200], and JSPS Fellows [Grant Number 20J20108].

Availability of data and materials
The data supporting the findings of this study are available from the corresponding author upon reasonable request.

Declarations

Competing interests
The authors declare that they have no competing interests.

Received: 2 September 2022 Accepted: 28 March 2023
Published online: 17 April 2023

References

Baron G, Ungemach P. European geothermal drilling experience-problem areas and case studies. In: International geothermal drilling and completions technology conference. Albuquerque, NM, USA. 1981. p. 24.

Batini F, Bertini G, Bottai A, Burgassi P, Cappetti G, Gianelli G, Puxeddu M. San Pompeo 2 deep well: a high temperature and high-pressure geothermal system. In: Strub A, Ungemach P, editors. European geothermal update: Proceedings of the 3rd international seminar on the results of EC geothermal energy research. 1983. p. 341–53.

Bertani, R, Büsing, H, Buske, S, Dini, A, Hjelstuen M, Luchini, M, Manzella, L, Nybo, R, Rabbel, W, Serniotti, L. and the DESCRAMBLE Science and Technology Team. The First Results of the DESCRAMBLE Project, PROCEEDINGS, 43rd Workshop on Geothermal Reservoir Engineering Stanford University. Stanford. California. Feb 12–14, 2018.

Chaki S, Takarli M, Agbodjan WP. Influence of thermal damage on physical properties of a granite rock: Porosity, permeability and ultrasonic wave evolutions. Constr Build Mater. 2008;22:1456–61.

Cox SF. The application of failure mode diagrams for exploring the roles of fluid pressure and stress states in controlling styles of fracture-controlled permeability enhancement in faults and shear zones. Geofluids. 2010;10:217–33.

Deichmann N, Giardini D. Earthquakes Induced by the stimulation of an enhanced geothermal system below basel (Switzerland). Seismol Res Lett. 2009;80(5):784–98.

Elders WA, Friðleifsson G, Albertsson A. Drilling into magma and the implications of the Iceland deep drilling project (IDDP) for high-temperature geothermal systems worldwide. Geothermics. 2014;49:111–8.
Espinosa-Paredes G, Garcia-Gutierrez A. Estimation of static formation temperatures in geothermal wells. Energy Conv Manag. 2003;44(8):1343–55.
Fournier RO. The transition from hydrostatic to greater than hydrostatic fluid pressure in presently active continental hydrothermal systems in crystalline rock. Geophys Res Lett. 1991;18(5):955–8.
Friðleifsson GO, Elders WA. The Iceland deep drilling project: a search for deep unconventional geothermal resources. Geothermics. 2005;34:269–85.
Friðleifsson GO, Elders WA. The Iceland deep drilling project geothermal well at reykjanes successfully reaches its supercritical target. Geotherm Resour Counc Bull. 2017;46:30–3.
Friðleifsson GO, Elders WA, Albertsson A. The concept of the Iceland deep drilling project. Geothermics. 2014;49:2–8.
Friðleifsson GO, Albertsson A, Stefansson B, Gunnlaugsson E, Adalsteinsson H. Deep Unconventional Geothermal Resources: a major opportunity to harness new sources of sustainable energy. In: Proceeding. 20th World Energy Conference Rome. World Energy Council. 2007. p. 21.
Garcia J, Hartline C, Walters M, Wright M, Rutqvist J, Dobson PF, Jeanne P. The Northwest Geysers EGS demonstration project, California: part 1: characterization and reservoir response to injection. Geothermics. 2016;63:97–119.
Goto R, Watanabe N, Sakaguchi K, Miura T, Chen Y, Ishibashi T, Pramudyo E, Parisio F, Yoshioka K, Nakamura K, Komai T, Tuchiya N. Creating cloud-fracture network by flow-induced microfracturing in superhot geothermal environment. Rock Mech Rock Eng. 2021;54:2959–74.
Goto R, Sakaguchi K, Parisio F, Yoshioka K, Pramudyo E, Watanabe N. Wellbore stability in high-temperature granite under true triaxial stress. Geothermics. 2022;100: 102334.
Grant MA, Clearwater J, Quinão J, Bixley PF, Brun ML. Thermal stimulation of geothermal wells: a review of field data. In: Proceedings, 38th Workshop on geothermal reservoir engineering. Stanford. Stanford University. 2013.
Griffith AA. Theory of rupture. In: Proceedings of the First International Congress on Applied Mechanics (eds Biezeno CB, Burgers JM). J Waltman Delft. 1924. p. 55–63.
Grigoli F, Scarabello L, Böse M, Weber B, Wiemer S, Clinton JF. Pick- and waveform-based techniques for real-time detection of induced seismicity. Geophys J Int. 2018;213:868–84.
Häring MO, Schanz U, Ladner F, Dyer BC. Characterisation of the Basel 1 enhanced geothermal system. Geothermics. 2008;37:469–95.
Heuze FE. High-temperature mechanical, physical and thermal properties of granitic rocks—a review. Int J Rock Mech Min Sci Geomech Abstr. 1983;20(1):3–10.
Jaeger JC, Cook NGW. Fundamentals of rock mechanics. 3rd ed. London: Chapman and Hall; 1979.
Jin P, Hu Y, Shao J, Zhao G, Zhu X, Li C. Influence of different thermal cycling treatments on the physical, mechanical and transport properties of granite. Geothermics. 2019;78:118–28.
Kaneta K, Mukuhira Y, Ito T. Numerical thermo-elastic stimulation for change in fracture aperture associated with cold fluid injection. GRC Transactions. 2014;38:301–4.
Kang F, Li Y, Tang C, Huang X, Li T. Competition between cooling contraction and fluid overpressure on aperture evolution in a geothermal system. Renew Energy. 2022;186:704–16.
Kato O, Doi N, Sakagawa Y, Uchida T. Fracture systematics in and around well WD-1, Kakkonda geothermal field. Japan Geothermics. 1998;27(5–6):609–29.
Kim KH, Ree JH, Kim YH, Kim S, Kang SY, Seo W. Assessing whether the 2017 Mw 5.4 pohang earthquake in South Korea was an induced event. Science. 2018;360:1007–9.
Kinoshita N, Abe T, Wakabayashi N, Ishida T. Mechanical properties of rock at high temperatures. Doboku Gakkai Ronbunshu. 1997;1997(561):151–62.
Liu B, Suzuki A, Watanabe N, Ishibashi T, Sakaguchi K, Ito T. Fracturing of granite rock with supercritical water for superhot geothermal resources. Renewable Energy. 2022;184:56–67.
Moore DE, Lockner DA, Byerlee JD. Reduction of permeability in granite at elevated temperatures. Science. 1994;265:1558–61.
Morrow CA, Moore DE, Lockner DA. Permeability reduction in granite under hydrothermal conditions. J Geophys Res. 2001;106:30551–60.
NEDO (New Energy and Industrial Technology Development Organization) FY 1995 report of the deep geothermal resources survey project. 887pp. 1996.
Parisio F, Vilarrasa V, Wang W, Kolditz O, Nagel T. The risks of long-term re-injection in supercritical geothermal systems. Nat Commun. 2019;10:1–11.
Parisio F, Lehmann C, Nagel T. A model of failure and localization of basalt at temperature and pressure conditions spanning the brittle-ductile transition. J Geophys Res Solid Earth. 2020;125:11.
Pramudyo E, Goto R, Watanabe N, Sakaguchi K, Nakamura K, Komai T. CO2 injection-induced complex cloud-fracture networks in granite at conventional and superhot geothermal conditions. Geothermics. 2021;97: 102265.
Ruggieri G, Gianelli G. Fluid inclusion data from the Carboli 11 well, Larderello geothermal field. Italy: Italy. World Geothermal Congress; 1995.
Saishu H, Okamoto A, Tsuchiya N. The significance of silica precipitation on the formation of the permeable-impermeable boundary within earth's crust. Terra Nova. 2014;26(4):253–9.
Secor DT. Role of fluid pressure in jointing. Am J Sci. 1965;263:633–46.
Shen Y, Hou X, Yuan J, Xu Z, Hao J, Gu L, Liu Z. Thermal deterioration of high-temperature granite after cooling shock: multiple-identification and damage mechanism. Bull Eng Geol Environ. 2020;79:5385–98.
Shimada S, Hokao Z. Thermal piercing simulation—an attempt to estimate thermal piercing rate and thermal cutting depth. J Min Metall Inst Jpn. 1980;96(1113):795–801.
Siratovich PA, Villeneuve MC, Cole JW, Kennedy BM, Bégué F. Saturated heating and quenching of three crustal rocks and implications for thermal stimulation of permeability in geothermal reservoirs. Int J Rock Mech Min Sci. 2015;80:265–80.

Smith R, Shaw H. Igneous-related geothermal systems. In: White, D. and Williams, D., editors. Assessment of geothermal resources of the United States—1975. U.S. Geological Survey Circular. 1975 726: 58–83.
Smith R, Shaw H. Igneous-related geothermal systems. In: Muffler, L., editor. Assessment of geothermal resources of the United States, 1978. U.S. Geological Survey Circular. 1979. 790: 12–7.
Steingrimsson B, Gudmundsson A, Franzson H, Gunnlaugsson E. Evidence of a supercritical fluid at depth in the Nesjavellir field. In: Proceedings 15th Workshop on Geothermal Reservoir Engineering. Stanford: Stanford University. 1990. p. 8.
Sun Z, Jiang C, Wang X, Zhou W, Lei Q. Combined effects of thermal perturbation and in-situ stress on heat transfer in fractured geothermal reservoir. Rock Mech Rock Eng. 2021;54:2165–81.
Sun Z, Zhang X, Xu Y, Yao J, Wang H, Lv S, Sun Z, Huang Y, Cai M, Huang X. Numerical simulation of the heat extraction in EGS with thermal-hydraulic-mechanical coupling method based on discrete fractures model. Energy. 2017;82:20–33.
Tester JW, Anderson BJ, Batchelor AS, Blackwell DD, DiPippo R, Drake EM, Garnish J, Livesay B, Moore MC, Nichols K, Petty S, Toksöz MN, Veatch RW Jr. The future of geothermal energy in the 21 century impact of enhanced geothermal systems (EGS) on the United States. Cambridge: MIT Press (MA); 2006.
Tsuchiya N, Hirano N. Chemical reaction diversity of geofluids revealed by hydrothermal experiments under sub- and supercritical states. Isl Arc. 2007;16(1):6–15.
Tsuchiya N, Yamada R, Uno M. Supercritical geothermal reservoir revealed by a granite-porphyry system. Geothermics. 2016;63:182–94.
Tullis J, Yund RA. Experimental deformation of dry Westerly granite. J Geophys Res. 1977;82:5705–18.
Violay M, Heap MJ, Acosta M, Madonna C. Porosity evolution at the brittle-ductile transition in the continental crust: Implications for deep hydro-geothermal circulation. Sci Rep. 2017;7:7705.
Watanabe N, Numakura T, Sakaguchi K, Saishu H, Okamoto A, Ingebritsen SE, Tsuchiya N. Potentially exploitable supercritical geothermal resources in the ductile crust. Nat Geosci. 2017a;10(2):140–4.
Watanabe N, Egawa M, Sakaguchi K, Ishibashi T, Tsuchiya N. Hydraulic fracturing and permeability enhancement in granite from subcritical/brittle to supercritical/ductile conditions. Geophys Res Lett. 2017b;44:5468–75.
Watanabe N, Sakaguchi K, Goto R, Miura T, Yamane K, Ishibashi T, Chen Y, Komai T, Tsuchiya N. Cloud-fracture networks as a means of accessing superhot geothermal energy. Sci Rep. 2019;9:939.
Watanabe N, Saito K, Okamoto A, Nakamura K, Ishibashi T, Saishu H, Komai T, Tsuchiya N. Stabilizing and enhancing permeability for sustainable and profitable energy extraction from superhot geothermal environments. Appl Energy. 2020;260: 114306.
Watanabe N, Abe H, Okamoto A, Nakamura K, Komai T. Formation of amorphous silica nanoparticles and its impact on permeability of fractured granite in superhot geothermal environment. Sci Rep. 2021;11:5340.
Watanabe K, Watanabe N, Watanabe N, Sakaguchi K, Aichi M, Ouchi H, Asanuma H. A numerical study on the creation of artificial supercritical geothermal reservoirs by hydraulic fracturing. Geothermics. 2022;105: 102500.
Weis P, Driesner T, Heinrich CA. Porphyry-copper ore shells form at stable pressure-temperature fronts within dynamic fluid plumes. Science. 2012;338:1613–6.

Publisher's Note